

Scatterfield microscopy of 22 nm node patterned defects using visible and DUV light

Bryan M. Barnes*, Yeung-Joon Sohn, Francois Goasmat, Hui Zhou, and Richard M. Silver
Semiconductor and Dimensional Metrology Division, Physical Measurement Laboratory,
National Institute of Standards and Technology,
100 Bureau Dr. MS 8212, Gaithersburg, MD USA 20899-8212

Abraham Arceo
SEMATECH Advanced Metrology Division
Albany, NY

ABSTRACT

Smaller patterning dimensions and novel architectures are fostering research into improved methods of defect detection in semiconductor device manufacturing. This experimental study, augmented with simulation, evaluates scatterfield microscopy to enhance defect detectability on two separate 22 nm node intentional defect array wafers. Reducing the illumination wavelength nominally delivers direct improvements to detectability. Precise control of the focus position is also critical for maximizing the defect signal. Engineering of the illumination linear polarization and incident angle are shown to optimize the detection of certain highly directional defects. Scanning electron microscopy verifies that sub 15 nm defects can be measured experimentally using 193 nm wavelength light. Techniques are discussed for taking advantage of the complexities inherent in the scattering of highly directional defects within unidirectional patterning. Although no one single set of parameters can be optimized to detect all defects equally, source optimization is shown to be a realistic path towards improved sensitivity.

Keywords: Defect detection, scatterfield optical microscopy, illumination optimization, bright-field microscopy, dark-field microscopy

1. INTRODUCTION

The continued vitality of high volume semiconductor manufacturing is challenged by the need for accurate defect inspection at ever-decreasing critical dimensions (CDs). Optimizations of conventional brightfield microscopy techniques are required, as well as alternatives. The National Institute of Standards and Technology (NIST) has been addressing this manufacturing need by evaluating optical techniques such as scatterfield optical microscopy, a combination of scatterometry and high magnification imaging to inspect three-dimensional scattered fields. Such fields, which are perturbed in the presence of patterned defects, are observable through differential imaging.

Previously reported [1] simulations of the detectability of certain defect types as a function of incident angle for the 65 nm and 32 nm node SEMATECH Intentional Defect Arrays (IDAs) have indicated that the defect-free patterns of the 32 nm node IDA are much more unidirectional than that the layouts in the 65 nm node IDA, reflecting recent trends in lithographic patterning. Within these 32 nm IDA targets, defects had either a low or a high directionality. Low directionality defects such as islands showed little increase in detectability as a function of incident angle. However, a highly directional bridge defect spanning two lines was much more detectable with off-axis illumination using a plane of incidence parallel to the primary features, thus perpendicular to the bridge. Recently, experiments compared defect detectability at the 32 nm node for a highly directional bridge defect as functions of defect size, incident angle, and polarization.[2] Supporting simulations at a 40 nm design rule using three-dimensional electromagnetic simulation packages that considered several parameters demonstrated angle- and polarization-resolved enhancements of defect sensitivity. Also shown was better detectability by changing the azimuthal angle. From this previous simulation work, the polarization, defect type, focus position, and incident angle can be determined to be crucial when seeking the optimum sensitivity for a specific defect, as no one set of optimized parameters improves the detection of all defects.

*bryan.barnes@nist.gov; phone 1 301 975-4396; fax 1 301 869-0822; www.nist.gov/pml/div683/grp02/htnsm.cfm

In this present work, the three-dimensional scattered field is used to enhance the detectability of defects at the 22 nm node. Experiments were used to verify trends found previously in simulation. Several experimental parameters were investigated including wavelength, focus position, incident angle, and polarization. The scatterfield optical microscopy technique was also pursued, highlighting the use of the entire three-dimensional scattered field. Recent electromagnetic simulation results using polarization, incident angle, and focus position were shown to facilitate the interpretation of experimental measurements. Measurements from two separate intentional defect arrays are discussed with these results.

2. SCATTERFIELD OPTICAL MICROSCOPY

A scatterfield optical microscope extracts information from a sample by probing the three-dimensional scattered field using the best attributes of both scatterometry and high magnification imaging. See Ref. [3] for details on the scatterfield technique and associated approaches to optimizing illumination. The interaction between the incident light and the sample is varied in scatterfield microscopy by adjusting the wavelength, linear polarization, and incident angle of the illumination. Focus position is an additional adjustable variable that is inherent in the use of high magnification imaging optics.

In this study, wavelength was varied by using two separate scatterfield optical tools, the NIST visible-light scatterfield microscope ($\lambda = 450$ nm) and the NIST 193 nm microscope ($\lambda = 193$ nm). Each tool was outfitted with linear polarizers and closed-loop piezoelectric actuators to allow polarized and focus-resolved measurements, respectively. Angle-resolved measurements on scatterfield tools are realized by designing the illumination column to feature Köhler illumination, a system by which each point on the source uniformly illuminates the field-of-view (FOV) from a particular incident angle. These microscopes have an optical column featuring an accessible plane that is conjugate to both the source and the objective's back focal plane. This conjugate back focal plane (CBFP) is where aperture(s) are placed and manipulated to permit specific ranges of angles through the illumination path. CBFP aperture position is mapped to the resultant angle of incidence as a calibration step for angle-resolved imaging. The full-field range of polar angles for the NIST visible-light scatterfield microscope is $\theta = 0^\circ$ to 72° , representing a numerical aperture (NA) of 0.95. For the NIST 193 nm microscope, a catadioptric objective lens limits the NA range from an inner value of NA = 0.11 to an outer value of NA = 0.74, corresponding to $\theta = 6^\circ$ to 47° .

Quantitative comparison between simulation and experimental results requires the simulation of multiple plane waves to account for the finite aperture(s) used for illumination. The number of simulations can typically be minimized by sampling about a mean angle. However, given the computationally intensive nature of defect simulations, here a single plane wave with a linear polarization illuminates the sample at a single angle of incidence and is reflected off these modeled targets.

3. THREE-DIMENSIONAL DEFECT SIMULATION

An in-depth simulation study in Ref. [2] of a 40 nm critical dimension (CD) target provided invaluable insight into optimizing the incident azimuthal angle (ϕ), polar angles (θ), and linear polarization to improve defect detection with respect to the patterning direction and defect orientation. A commercial finite element method (FEM) [4] Maxwell's equations solver software package was employed, as the modeling of scattering from defect targets requires the use of three-dimensional electromagnetic simulators. In this analysis, two sets of data were simulated, one with a patterned defect and one without. The result of each simulation is an aerial image. The defect-containing and defect-free images are subtracted to determine the difference in the scattered field as a result of the defect. This difference is the defect signal. To produce Fig. 1, forty-three simulation sets were performed and the absolute value of the differential image calculated. The absolute value image was reduced to a single mean value to provide a figure of merit (FOM) that is then plotted as a function of incident angle. The defect detectability should scale with the magnitude of the FOM.

In the middle of Figure 1 are four polar plots of the defect detectability FOM as functions of incident angle. The polarization and defect type for each plot can be determined by the labels at the top and left (*i.e.*, the upper right plot is for the "Bx"-like bridge defect and *s*-polarization). The directions of the *s*- and *p*-polarizations can be determined for these simulations using the angle diagram at right. Again, using the upper right plot as an example, the *s*-polarization at $\phi = 0^\circ$ is aligned along the direction of the lines and defect while at $\phi = 90^\circ$, the polarization is perpendicular to the lines and defect.

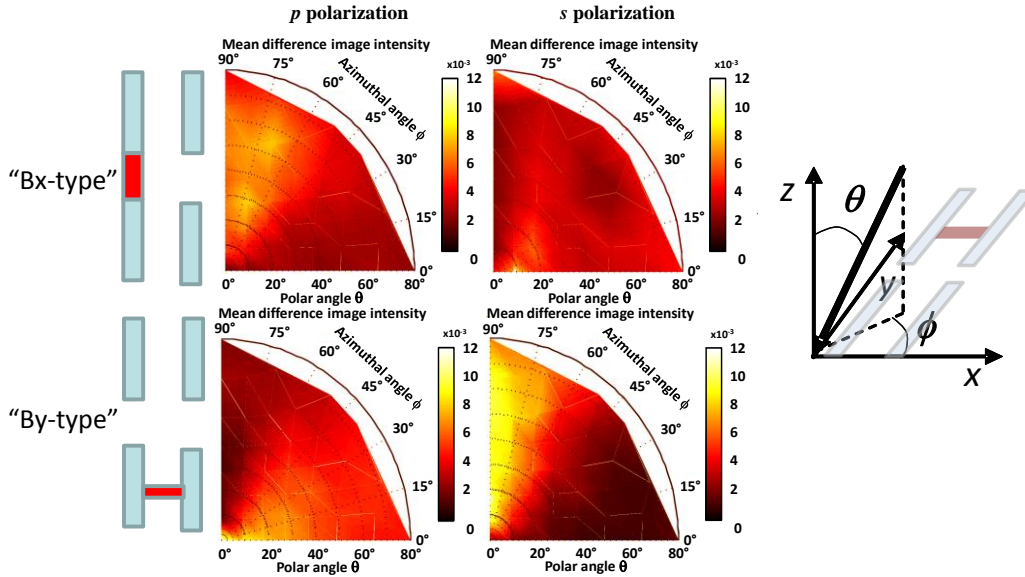


Figure 1. (left) Schematics of two types of highly directional bridge defects. The upper schematic roughly correlates to the SEMATECH defect “Bx,” the lower to defect “By.” (middle) A 2×2 matrix of plots corresponds to the four possible combinations of p - and s -polarization and the two defect types shown at left. Plots are of a defect detectability FOM described in the text shown as a function of polar and azimuthal angle. (right) Definitions of polar and azimuthal angle relative to the simulation layout. These simulations were performed for a 40 nm CD illuminated with $\lambda = 193$ nm light. Graphs adapted from Ref. [2].

These plots show that the strongest detectability should be for the “By”-type defect, illuminated using linearly polarized light aligned with the defect but across the patterned lines, using angle-resolved incident light with an incident plane along the lines and across the bridge. For the “Bx”-type defect, the detectability is strong when illuminated using linearly polarized light that is aligned along the defect and the patterned lines, using angle-resolved incident light with an incident plane along the lines and bridge.

Using previously developed through-focus differential imaging methods,[5] simulation work has also been performed to evaluate the role of focus position on the detectability of defects at the 22 nm node. Simulations were performed using a finite difference time domain (FDTD) [6] simulation package developed in-house. SEMATECH-provided “Bx” and “By” layouts and materials stacks were used to simulate the focus-resolved series of differential images shown in Fig. 2. The simulation domain size in the x - y plane was $3.2 \mu\text{m} \times 3.2 \mu\text{m}$, a size chosen to allow several “buffer” unit cells that did not contain defects to surround the defect-containing unit cell. These results are for single plane waves with $\lambda = 193$ nm normally incident onto the targets. The “Bx” structure is shown in the left column in Fig. 2; the “By” structure is on the right. The CD for both defects is 8.8 nm (40 % of design rule). The incident light is linearly polarized and aligned with the bridge direction. Positions along the z -axis are relative to the substrate, with $z = 0$ nm set at the base of the patterned features.

Several observations can be made from these through-focus simulations. First, in this comparison, the defect signal from the “By” defect is stronger than from the “Bx” defect. Second, for both, the beneficial effects of linearly polarized light are not affected by changes in focus position, as simulations with the linear polarization aligned across each bridge (not shown) demonstrated a smaller defect signal at all focus positions. Third, for these defects at this wavelength, the defect signal is highly localized in the x - y plane for a z range from -200 nm to 400 nm. Below and above this range, the signal intensity weakens but spreads laterally. Fourth, the relative strength of the defect signal outside this optimal z range must not be overemphasized. As stated, the length of each side of the x - y simulation domain size is $3.2 \mu\text{m}$, which is greater than 16 wavelengths. Still, at 1000 nm above the substrate, the ripples from the defect signal begin to interact with the periodic “copies” of the defect that this FDTD implementation assumes are in adjacent domains. This repetition is unavoidable as the periodic boundary condition is necessary to simulate the underlying pattern and can be mitigated

by increased domain sizes. These focus-resolved simulations as well as the angle-resolved simulations were used to facilitate the interpretation of the following experimental results.

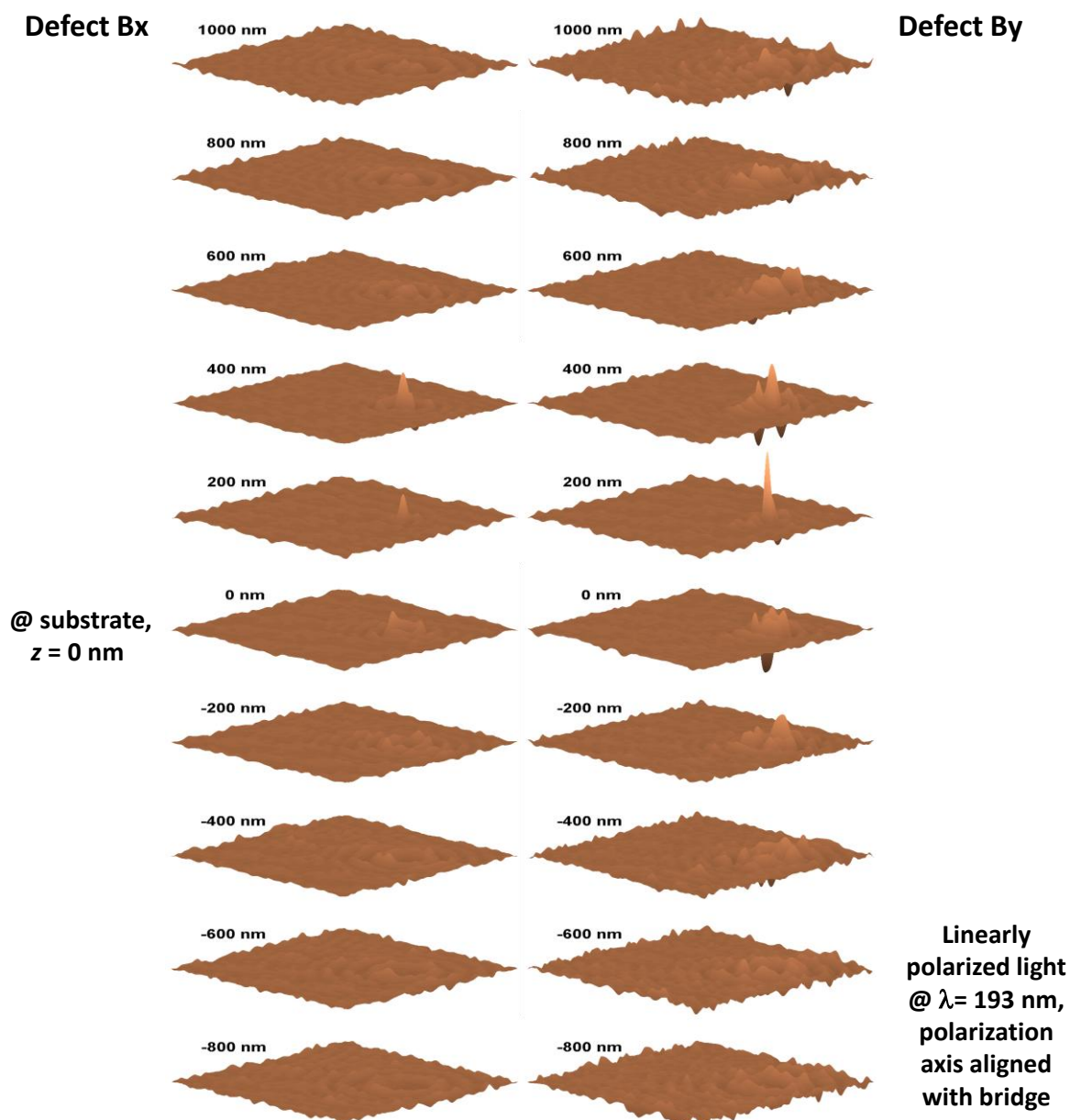


Figure 2. Focus-resolved simulated differential images of “Bx” (left column) and “By” (right column) defects with critical dimensions of 40 % of the 22 nm design rule (8.8 nm). Simulations were performed for $\lambda = 193$ nm light using an in-house finite difference time domain (FDTD) model. Because these simulations assume periodic boundary conditions, interference among the periodic defects has been reduced by introducing a buffer of unit cells with no defects. Here, defect signals are spatially localized and relatively strong for a z -range from -200 nm below the substrate to +400 nm above.

4. EXPERIMENTAL MEASUREMENTS OF INTENTIONAL DEFECT ARRAYS

4.1 Overview

For this initial study at the 22 nm node, two IDA wafer coupons were measured. The first coupon had printed features made of photolithographic resist on silicon (hereafter the resist wafer). This wafer was measured extensively on the NIST visible-light scatterfield microscope ($\lambda = 450$ nm). Additional measurements were not possible using $\lambda = 193$ nm light due to the interaction of the resist with the highly focused light at the objective lens. The second coupon was etched using e-beam lithography (hereafter the e-beam etch wafer). Due to time constraints, this wafer was inspected on only the NIST 193 nm microscope.

While the wafers and wavelengths were different, several commonalities tie the two experiments together. Both were designed for the 22 nm node, and both involved measurements on scatterfield-capable platforms. Both wafers offer a matrix of defect types and defect sizes nominally scaled to the 22 nm design rule. Island (“A”) and (“Bx,” “By”) bridge defects were measured on both (see Figure 3).



Figure 3. Schematics of an island (“A”) and two bridge (“Bx,” “By”) defects found on 22 nm node SEMATECH Intentional Defect Array (IDA) wafers.

At each pairing of defect size and type, an image of the defect is acquired with a second image collected nearby so that one image can be subtracted from another. This process yields a differential image for extracting the signal from this defect.

Before aligning each defect-reference pair together, every image was processed using discrete Fourier transforms. Low frequency filters were applied to each image, removing constant backgrounds and large area variations. For images of the 22 nm node resist wafer, a high frequency filter was applied to isolate the repetitive structure of the defects from the noise in the images. For images from the resist wafer, a more sophisticated algorithm preserved the inherent repetition in the image while limiting the extraneous noise. After inverse discrete Fourier transformation of the filtered images, the defect image and reference image are aligned using components of the Enhanced Correlation Coefficient (ECC) algorithm of Evangelidis and Psarakis.[7] In the full ECC treatment, a matrix is produced to warp one image to maximize its correlation with a second image. Here, only the lateral shift elements of this matrix are used to perform the

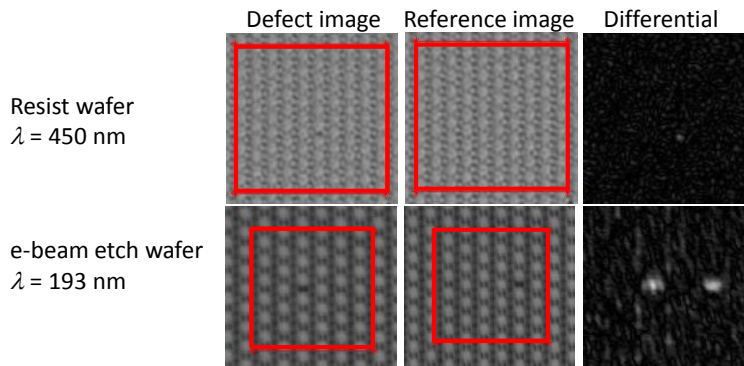


Figure 4. Defect detection for bridge defect “Bx” of nominal size 22 nm. (top row) The defect image shows a dark spot indicating a defect. The reference image was collected after shifting laterally 30 μm , thus successful differential images will have a single defect signal. (bottom row) The “reference” image is shifted two rows relative to the defect image, thus successful differential images will have two defect signals per image.

sub-pixel interpolation required to align the images, leaving the shape and dimensions of the images intact. Examples of the filtered images and ECC-corrected, absolute value differential images appear in Fig. 4.

For both experiments, qualitative presentations of the differential images are made to demonstrate defect detectability. A more comprehensive study is required to fully explore the complex interactions among defect type, focus position, incident angle, and polarization. Even though rigorous treatment of these images is underway, including a well-defined metric for defect detection and signal-to-noise analysis, this qualitative presentation suggests strong trends for enhancing defect inspection using combinations of these four parameters.

4.2 22 nm node resist wafer

Although the two measurement efforts were similar, the experimental design was varied to broadly explore the interactions among incident angle, wavelength, polarization, and focus position. For initial measurements of the resist wafer, data acquisition was concentrated on focus-resolved measurements using full-field illumination and linearly polarized light. For the e-beam resist wafer, full-field and angle-resolved measurements were performed, also using linearly polarized light.

Polarization effects are immediately apparent in Fig. 5, which shows measurements of the two bridge defects, “Bx” and “By,” on the resist wafer. The linear polarization for each row is listed to the left of the figure. At the far right, the largest defects are observed for all polarizations, *i.e.*, “300-Bx,” which is nominally 300 % of the design rule or 66 nm. The position of the defect in the FOV varies little as size is decreased. Since all images here are shown at the same intensity scale, it can be seen that the strength of the signal decreases with size until it is no longer visible. Following the top row, where the light is linearly polarized in the same direction as the length of the bridge, the “Bx” defect is clearly visible to “100-Bx,” while still faintly visible down to “70-Bx.” However, for the second row and orthogonal polarization, the defect completely disappears by “80-Bx.” In the fourth row, the “By” defect is clearly visible to “160-Bx,” persists faintly down to “70-By,” then in the third row, its signal falls off dramatically below “200-By.” Here also, linear polarization in the direction along the bridge yields the greater detectability. Based on the design rule and these qualitative observations, polarization enables the observation of nominally 15.4 nm defects using $\lambda = 450$ nm light.

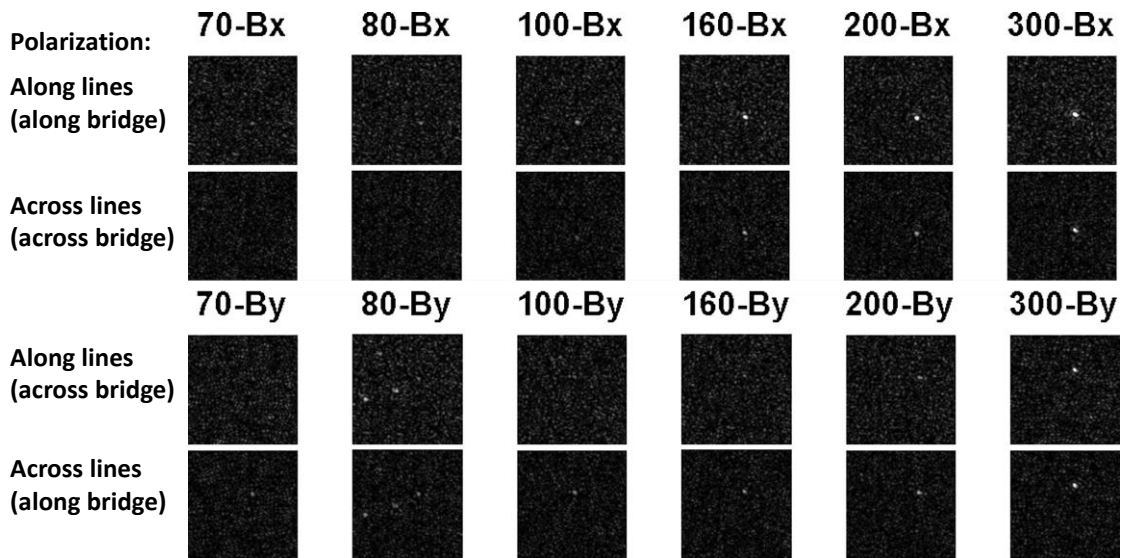
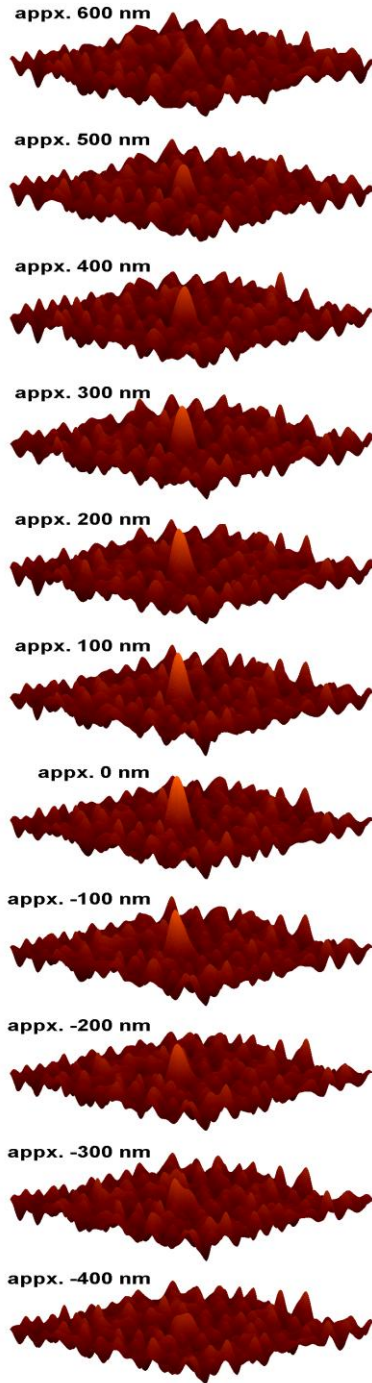
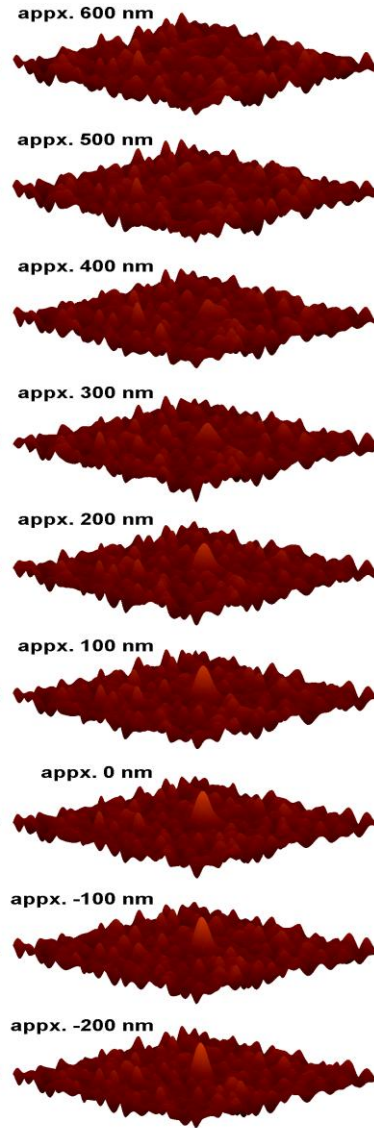


Figure 5. Absolute value differential images of defects on the 22 nm resist wafer measured with linearly polarized $\lambda = 450$ nm light. Labels indicate percentage of design rule and defect shown (*i.e.*, “70-By” is a “By” defect nominally sized 70 % of 22 nm, or 15.4 nm.) Polarization axis is shown at the far left. Defect detectability is improved by aligning the polarization axis along the direction of the bridge as defined in Fig. 3. Unintentional defects are near the “80-By” defect.

Defect Bx



Defect By



**z=0 defined by
applying a
gradient-based
focus metric on
the reference
image.**

**Linearly polarized light @ $\lambda = 450$ nm,
polarization axis aligned with bridge**

Figure 6. Experimental focus-resolved differential images for defects “Bx” and “By” at 100 % of the design rule (nominal size, 22 nm) using $\lambda = 450$ nm illumination. For the “Bx” defect (left column), the defect signal appears, then disappears over a focus range of $z = -400$ nm to 600 nm. Unlike the previous figure, these differential images are not plotted as absolute values.

Connecting the results of Fig. 1, which are presented as functions of angle, with the results of full-field experimental data is not straightforward. In experiments, the full-field is polarized using a single optical element yielding x - or y -polarization as defined by the axes of the CBFP. The physical optics involved can complicate the conversion of x - and y -polarization to s - and p -polarization at the sample [8]; the data in Fig. 1 can be applied by approximating that the s - and p -polarizations transverse the illumination path unperturbed. Looking at the upper row for “Bx”-type defects, the two graphs show that p -polarization incident at $\phi = 90^\circ$ enhances detectability; this is less so for s -polarization incident at $\phi = 0^\circ$. Both p -polarization at $\phi = 90^\circ$ and s -polarization at $\phi = 0^\circ$ are aligned along the lines and bridges for the “Bx” defect, correlating well with the basic trends in the experimental data in Fig. 5. Likewise, for a “By”-type defect in the bottom row in Fig. 1, the stronger FOMs at both p -polarization at $\phi = 0^\circ$ and s -polarization at $\phi = 90^\circ$ are aligned along the bridge and across the lines. This also compares favorably with the basic trends in the experimental data for the “By” defect.

Focus-resolved defect detection was investigated using experimental differential images of the 100 % design rule “Bx” and “By” defects collected at $\Delta z = 50$ nm focus increments. Figure 6 plots three-dimensional renderings of defect differential images as functions of focus height, for which the position in z has been approximated relative to the best focus achieved on the reference image using a gradient-based focus metric. The x - y dimensions of these images are approximately $12 \mu\text{m} \times 12 \mu\text{m}$.

For both the “Bx” and “By” defects here, linearly polarized illumination parallel to the bridges yielded better detectability throughout the focus range; therefore, data from illumination that is linearly polarized orthogonal to the bridges are not shown. Again, this suggests that the strong defectivity signal from linearly polarized light is not affected by changes in focus position. The “Bx” defect emerges, persists, and disappears over a z -range from -400 nm to 600 nm using $\lambda = 450$ nm light. The limited region is larger than, but reminiscent of, the limited z range suggested by Fig. 2 in the $\lambda = 193$ nm simulation. These focus-resolved data also emphasize the importance of noise on the images and in the image alignment. All plots in Fig. 6 use the same intensity scale; “Bx” appears to have the stronger signal. However, the noise in the “By” column is demonstrably better, most likely due to the relative success of the image alignment algorithm. Due to the signal-to-noise ratio, a quantitative analysis would likely indicate that the “By” defect is more detectable. Simulations with proper noise models and experiments with improved image alignment will be required to understand whether these limited observations are indicative of trends in the focus-resolved data.

4.3 22 nm node e-beam etched IDA

Full-field and angle-resolved measurements were performed on the e-beam etched wafer using linearly polarized light from the NIST 193 nm microscope. In Fig. 7, absolute value differential images are presented for the “Bx” and “By” defects for design rules from 25 % to 100 %. The most noticeable features in these images are the two defect signals (explained in Fig. 4) and the higher noise level as compared to the $\lambda = 450$ nm measurements. These variations are most likely due to speckle and intensity variations in the defect and reference images that the Fourier filtering could not remove. The NIST 193 nm microscope [9] has an ArF excimer laser as its light source, and although most coherence is broken using a rotating diffuser at the source plane, the light is still partially coherent. In addition, intensity levels from excimer lasers fluctuates between images. In contrast, the $\lambda = 450$ nm data were acquired using an incoherent light-emitting diode. Despite these factors, defect detection is still clearly achieved using $\lambda = 193$ nm light down to the “Bx-25” and “By-40” defects using polarized light.

The most notable result from Fig. 7 is that the optimal polarization axis apparently switches from an orientation parallel with the bridge to perpendicular to the bridge. The data show that there is no single prescription for optimizing the defect detectability of a bridge defect. While trends in individual situations are observed, the wavelength, process stack, and defect type must be fully accounted for to determine the best method to improve defect detectability.

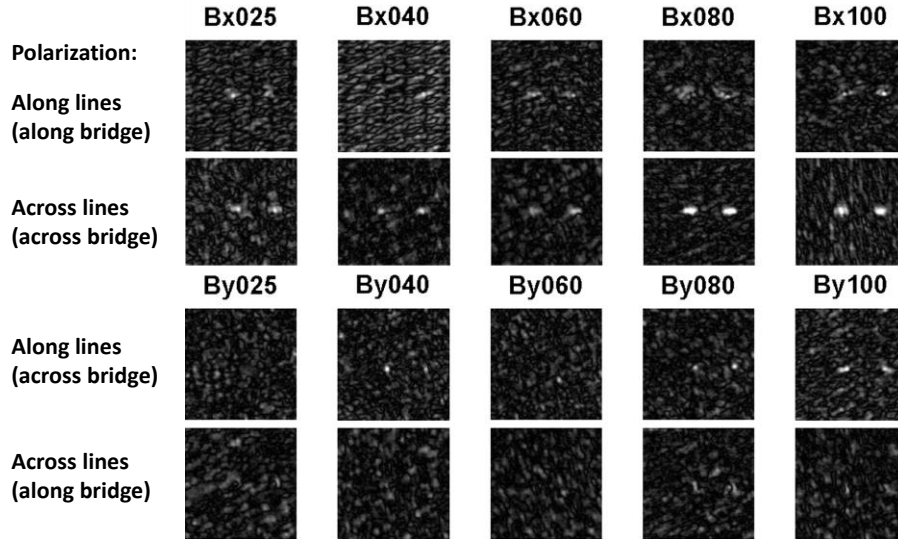


Figure 7. Absolute value differential images of defects on the 22 nm e-beam etched wafer measured with linearly polarized $\lambda = 193$ nm light. Similar to Fig. 5, labels indicate percentage of the design rule and defect shown. Unlike Fig. 5, defect detectability is improved by aligning the polarization axis across the direction of the bridge as defined in Fig. 3. In addition to noise from misalignment, speckle and laser intensity variation affect these differential images.

A dipole aperture was added to the CBFP of the NIST 193 nm microscope to experimentally determine the benefits to defect detection of angle-resolved illumination using a relatively simple engineering solution. On the left in Fig. 8 is an image of the dipole illuminator as imaged previously at a Fourier plane in the collection path. This fixed dipole aperture yields an illumination $NA = 0.58$ to 0.74 ($\theta = 36^\circ$ to 47°) with an azimuthal angular width of $\Delta\phi = \pm 45^\circ$. In this work, the dipole was oriented with the azimuthal angles on average parallel to the dominant lines. Both “Bx” and “By” were measured, with “By” shown in Fig. 8. For the “Bx” defect, the angles on average converged along the direction of the bridge, while for the “By” defect, the angles converged on average from both sides of the bridge as illustrated in the middle of Fig. 8. The “By25” defect is now faintly observed, but all nominally larger “By” defects are clearly seen.

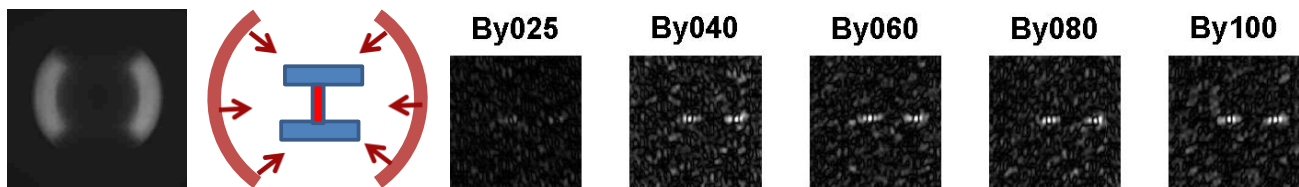


Figure 8. Improved detectability of the “By” defect using dipole illumination. (left) Fourier plane image of dipole illuminator. (middle) Schematic of orientation with respect to the defect. (right) With dipole illumination, all “By” defects are observed.

To quantify the CDs of the defects observed on the e-beam etched wafer, selected defects were also measured using scanning electron microscopy (SEM). SEM images were collected for the three smallest nominal “Bx” and “By” defects. Images of these defects and their initial measurements are given in Fig. 9. These measurements show that the narrowest defect was not always the defect designed to be 25 % of the design rule. For the “By” defect, the smallest defect detected was “Bx60” with a $CD = 17 \text{ nm} \pm 2 \text{ nm}$. While the CD for “Bx60” is marginally smaller than that for “Bx40,” the latter bridge is connected. Therefore, the smallest connected “Bx” bridge observed has a $CD = 15 \text{ nm} \pm 2 \text{ nm}$ as measured by SEM.

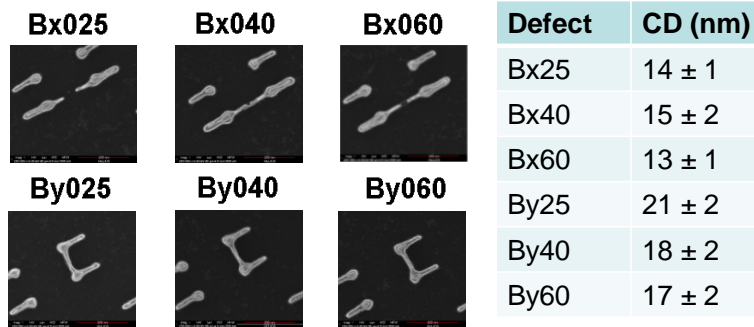


Figure 9. (left) Scanning electron microscope (SEM) images of the three nominally smallest bridge defects on the 22 nm node e-beam etched wafer. For the “Bx” defect, only the 40 % design rule bridge is contiguous. All “By” bridges are connected. (right) Table of measured defect critical dimensions (CDs) with their uncertainties ($k = 2$).

Because they were not inspected as thoroughly as the bridge defects, data from other defects on the 22 nm node e-beam etched wafer are preliminary. In Fig. 10, the optical difference image and the SEM image of the 160 % design rule island (“A”) defect are shown. Neither optical microscopy nor SEM could detect defects below the 100 % design rule, indicating this is the smallest island available.

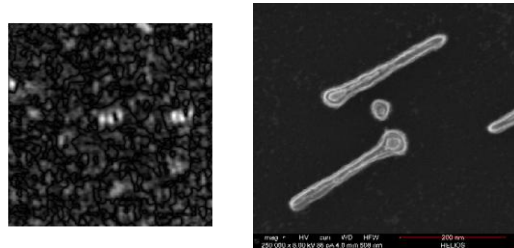


Figure 10. Optical $\lambda = 193$ nm difference image (left) and SEM image (right) of an e-beam etched IDA island defect “A.” The optical image was collected using linear polarization oriented across the lines and dipole illumination. Neither SEM nor optical microscopy could detect defects below the 160 % design rule.

Line extensions “Cx” and “Cy” were also observed, as well as line breaks “J” and “K.” Figure 11 shows these defects in multiple sizes using optimized linear polarization. The “Cx” defect is not consistently observed below 100 % of the design rule. Both “Cy” and “J” are seen at the 80 % design rule (nominally 17.6 nm) with “K” observed at 60 % of the design rule (nominally 13.2 nm). These initial full-field images illustrate the various types of defects that must be observed and the continual efforts required to improve the detectability of various defects.

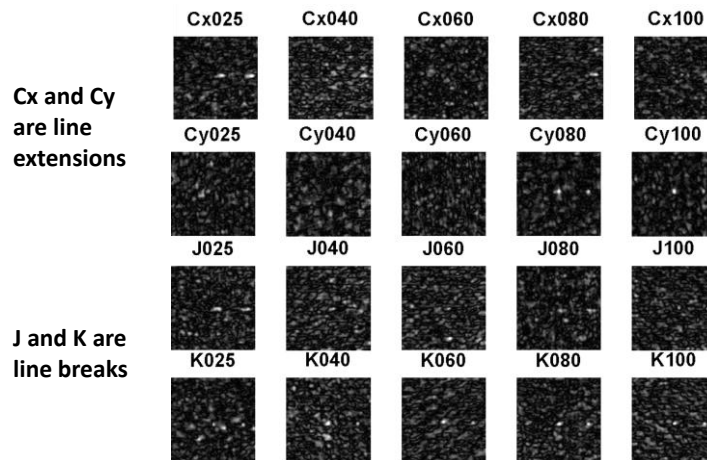


Figure 11. Initial differential image measurements of defects “Cx,” “Cy,” “J,” and “K.” Full-field illumination and optimized linear polarization have been used in these preliminary measurements. Polarization effects are strong for “Cy,” “J,” and “K.”

5. CONCLUSIONS AND FUTURE WORK

In simulations and experiments, scatterfield microscopy and optimized illumination have improved the defect detectability of features well below sub-wavelength dimensions by using the entire scattered field. Four specific parameters were varied experimentally to enhance defect analysis: linear polarization direction, focus position, incident angle, and illumination wavelength. Clearly detectability gains were evident for most defects in these IDAs by pairing each defect with an optimal polarization direction. With focus-resolved scanning, the best detectability may be found with slightly defocused images. Certain defects appear and disappear about an optimal point. The impact of the incident angle on detectability, as predicted in the simulations, was demonstrated using dipole illumination. Dipole illumination demonstrated gains when the illumination was engineered to the defect. Such simple techniques are good engineering solutions that can be readily applied; however, no one set of optimized parameters will capture all defects equally. Defects measured using 450 nm light were detected as small as 15 nm ($< \lambda / 20$). SEM measurements confirmed the defect detectability of bridges as narrow as 15 nm \pm 2 nm using 193 nm light ($< \lambda / 12$). Even smaller defects are expected to be detectable using this deep ultraviolet light.

ACKNOWLEDGEMENTS

The authors wish to thank the SEMATECH Advanced Metrology Division for access to the IDA wafers. We also thank Andras Vladar and Bin Ming for SEM measurements.

REFERENCES

- [1] R.M. Silver, B. M. Barnes, Y.-J. Sohn, R. Quintanilha, H. Zhou, C. Deeb, M. Johnson, M. Goodwin, and D. Patel, "The limits and extensibility of optical patterned defect inspection," Proc. SPIE 7638, 76380J (2010).
- [2] B. M. Barnes, R. Quintanilha, Y.-J. Sohn, H. Zhou, and R.M. Silver, "Optical illumination optimization for patterned defect inspection," Proc. SPIE 7971, 79710D (2011)
- [3] B. M. Barnes, R. Attota, R. Quintanilha, Y.-J. Sohn, and R. M. Silver, "Characterizing a scatterfield optical platform for semiconductor metrology," Meas. Sci. Technol. 22, 024003 (2011).
- [4] F. Schmidt, "An adaptive approach to the numerical solution of Fresnel's wave equation," IEEE J. Lightwave Technol. 11, 1425-1434 (1993).
- [5] R. M. Silver, R. Attota, B. Barnes, and H. Zhou, "A theoretical and experimental evaluation of scatterfield microscopy for use in patterned defect inspection," Sematech Tech Transfer Document, Feb. (2007).
- [6] A. Taflove, "Application of the finite-difference time-domain method to sinusoidal steady-state electromagnetic-penetration problems," IEEE Transactions on Electromagnetic Compatibility, EMC-22, 191-202 (1980).
- [7] G.D. Evangelidis and E. Z. Psarakis, "Parametric image alignment using enhanced correlation coefficient maximization," IEEE Trans. Pattern Analysis and Machine Intelligence 30, 1-8 (2008).
- [8] R. M. Silver, J. Qin, H. Zhou, B. M. Barnes, F. Goasmat, and R. Dixon, "Phase sensitive parametric optical metrology: Exploring the limits of 3-dimensional optical metrology," Proc. SPIE 8324 (2012).
- [9] Y.-J. Sohn, R. Quintanilha, B.M. Barnes, and R. M. Silver, "193 nm angle-resolved scatterfield microscope for semiconductor metrology," Proc. SPIE 7405, 74050R (2009).

The full description of the procedures used in this paper requires the identification of certain commercial products and their suppliers. The inclusion of such information should in no way be construed as indicating that such products or suppliers are endorsed by NIST or are recommended by NIST or that they are necessarily the best materials, instruments, software or suppliers for the purposes described.